Numerical study of shear-dependent non-Newtonian fluids in compliant vessels

A. Hundertmark-Zaušková*†, M. Lukáčová-Medviďová*‡

Abstract

The aim of this contribution is to present recent results on numerical modelling of non-Newtonian flow in compliant stenosed vessels with application in hemodynamics. We consider two models of shear-thinning non-Newtonian fluids and compare them with the Newtonian model. For the structure problem the generalized string equation for radial symmetric tubes is used and extended to a stenosed vessel. The global iterative approach to approximate the fluid-structure interaction is used. At the end we present numerical experiments for some non-Newtonian models, comparisons with the Newtonian model and the results for hemodynamic wall parameters; the wall shear stress and the oscillatory shear index.

keywords: non-Newtonian fluids, fluid-structure interaction, shear-thinning flow, hemodynamic wall parameters, stenosis

1 Introduction

Description of blood flow in human arteries is a very complex process. In recent years there is a growing interest in the use of mathematical models and numerical methods arising from other fields of computational fluid dynamics in the hemodynamics, see, e.g., [4], [6], [10], [13], [16], [19], [21], [22], [23], [24], [31] just to mention some of them.

Many numerical methods used for blood flow simulation are based on the Newtonian model using the Navier-Stokes equations. This is effective and useful, especially if the flow in large arteries should be modeled. However, in small vessels blood cannot be considered as the Newtonian fluid anymore. In capillaries the blood is even not a homogenized continuum and more precise models, for example mixture theories need to be used. But even in the intermediate-size vessels the non-Newtonian behavior of blood is demonstrable, see [25], [2] and the references therein. In fact, blood is a complex fluid showing several non-Newtonian properties, for example shear-thinning or viscoelasticity [29], [30] yield stress, stress relaxation [25]. The aim of this paper is to report on recent results concerning numerical modelling of shear-thinning flow in moving vessels with application in hemodynamics. We address the significance of non-Newtonian models for reliable hemodynamical modelling. In particular, we will show that the rheological properties of fluid have an influence on the wall deformation as well as on the hemodynamical wall indices, such as

*Institute of Numerical Simulation, Hamburg University of Technology, Hamburg, Germany
†Department of Mathematical and Numerical Analysis, Comenius University, Bratislava, Slovakia
‡corresponding author: lukacova@tu-harburg.de

the wall shear stress and oscillatory shear index. Consequently these models yield more reliable prediction of critical vessel areas, see also our previous preliminary study in [15].

The present paper is organized as follows. In Section 2 we describe mathematical model of shear thinning non-Newtonian fluid in a moving domain and present typical models for blood. Section 3 gives a detailed derivation of the generalized string model for cylindrical symmetric vessels with non-constant radius. In Section 4 we present theoretical results of well-posedness of weak solution for the coupled fluid-structure interaction problem, the detailed mathematical analysis goes behind the frame of the present paper and will be presented in our forthcoming paper [14]. The coupled fluid-structure interaction algorithm based on so-called global iterative method with respect to the domain deformation is described in Section 5. Section 6 is devoted to a detailed computational study of shear-thinning fluids in moving domains. Numerical experiments for viscosity data tested by Sequeira, Nadau [16] has been extended for fixed (solid) and moving vessels, both stenotic and straight. In hemodynamical wall indices new effects due to the fluid-structure interaction has been observed, see Section 6.1. Moreover in Section 6.2 an extensive numerical study for real physiological parameters is presented. We have considered physiological viscosity parameters as well as inflow data from iliac artery measurements. Additionally, we assume different material properties in stenotic regions in order to model accumulated plug. Finally the influence of different boundary conditions on the convergence of the complete method for rigid and moving domains is studied in Section 7.

2 Mathematical model: non-Newtonian fluid in a moving domain, hemodynamical indices

Consider a two-dimensional fluid motion governed by the momentum and the continuity equation

$$\begin{aligned} \rho\frac{\partial \boldsymbol{u}}{\partial t} + \rho\,(\boldsymbol{u}\cdot\nabla)\,\boldsymbol{u} - \operatorname{div}\left[2\mu(|D(\nabla\boldsymbol{u})|)D(\nabla\boldsymbol{u})\right] + \nabla p &= 0 \\ \operatorname{div}\boldsymbol{u} &= 0 \end{aligned} \tag{1}$$

with ρ denoting the constant density of fluid, $\boldsymbol{u} = (u_1, u_2)$ the velocity vector, p the pressure, $D(\nabla\boldsymbol{u}) = \frac{1}{2}(\nabla\boldsymbol{u} + \nabla\boldsymbol{u}^T)$ the symmetric deformation tensor and μ the viscosity of the fluid. The computational domain

$$\Omega(\eta) \equiv \{(x_1, x_2, t) :\ -L < x_1 < L,\ 0 < x_2 < R_0(x_1) + \eta(x_1, t),\ 0 < t < T\}$$

is given by a reference radius function $R_0(x_1)$ and the unknown free boundary function $\eta(x_1, t)$ describing the domain deformation. In this work we restrict ourselves to 2D domains. The fluid and the geometry of the computational domain are coupled through the following Dirichlet boundary condition

$$u_2(x_1, x_2, t) = \frac{\partial\eta(x_1, t)}{\partial t}, \quad u_1(x_1, x_2, t) = 0 \quad \text{on } \Gamma^w, \tag{2}$$

where $\Gamma^w = \{(x_1, x_2);\ x_2 = R_0(x_1) + \eta(x_1, t),\ x_1 \in (-L, L)\}$ is the deforming part of the boundary. With $\boldsymbol{n}$ we denote the unit outward normal vector to this boundary,

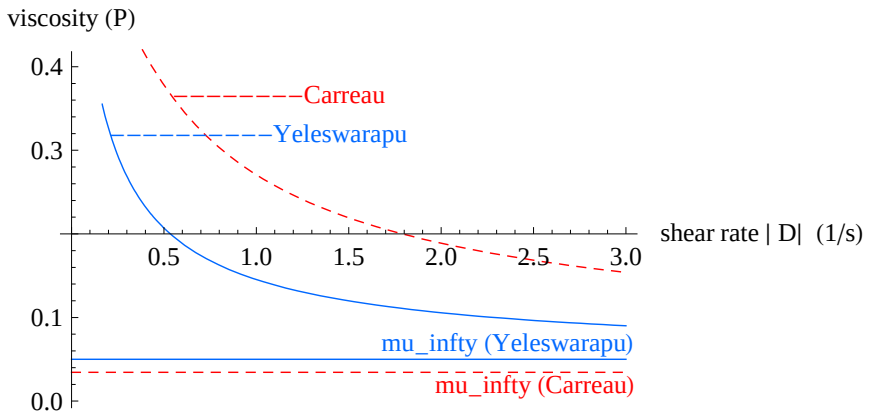

Figure 1: Viscosity function for both shear dependent models

$\boldsymbol{n} := (-\partial_{x_1}(R_0+\eta),1))/\sqrt{(\partial_{x_1}(R_0+\eta))^2+1}$. Moreover, the normal component of the fluid stress tensor provides the forcing term for the deformation equation of free boundary η, that will be introduced below.

In what follows we introduce non-Newtonian models that describe the shear thinning properties of blood. In the literature various non-Newtonian models for the blood flow can be found. In this paper we consider the so-called Carreau model [29] and the Yeleswarapu-viscosity model [29]. According to the Carreau model for the shear-thinning fluid, the viscosity function depends on the deformation tensor in the following way

$$\mu = \mu(D(\nabla \boldsymbol{u})) = \mu_\infty + (\mu_0 - \mu_\infty)(1 + |\gamma D(\nabla \boldsymbol{u})|^2)^q \tag{3}$$

for some given constants $q, \mu_0, \mu_\infty, \gamma$. According to [29] the physiological values for blood are $\mu_0 = 0.56P,\ \mu_\infty = 0.0345P,\ \gamma = 3.313,\ q = -0.322$. Note that in the case $q = 0$ the model reduces to the linear Newtonian model used in the Navier-Stokes equations.

The Yeleswarapu viscosity model reads

$$\mu = \mu(D(\nabla \boldsymbol{u})) = \mu_\infty + (\mu_0 - \mu_\infty)\frac{\log(1+\gamma|D(\nabla \boldsymbol{u})|)+1}{(1+\gamma|D(\nabla \boldsymbol{u})|)}. \tag{4}$$

The physiological measurements give $\mu_0 = 0.736P,\ \mu_\infty = 0.05P,\ \gamma = 14.81$ [29].

Several hemodynamical indices have been proposed in literature in order to measure the risk zones in blood vessel. They have been introduced to describe some mechanisms correlated to intimal thickening of vessel wall. Many observations show that one reason is the blood flow oscillations during the diastolic phase of every single heart beat. To identify the occlusion risk zones the *Oscillatory Shear Index* is usually studied in literature, see [23]

$$OSI := \frac{1}{2}\left(1 - \frac{\int_0^T \tau_w\, dt}{\int_0^T |\tau_w|\, dt}\right), \tag{5}$$

where $[0, T)$ is the time interval of a single heart beat ($T \approx 1sec$) and τ_w is the *Wall Shear Stress* (WSS) defined as

$$WSS := \tau_w = -\mathbf{T}_f \boldsymbol{n} \cdot \boldsymbol{\tau}. \tag{6}$$

Here $\mathbf{T}_f$ is the Cauchy stress tensor of fluid $\mathbf{T}_f = -p\mathbf{I} + 2\mu(|D(\nabla \boldsymbol{u})|)D(\nabla \boldsymbol{u})$, $\boldsymbol{n}$ and $\boldsymbol{\tau}$ are the unit outward normal and the unit tangential vector on the arterial wall Γ^w, respectively. OSI index measures the temporal oscillations of the shear stress pointwise without taking into account the shear stress behavior in an immediate neighborhood of a specific point.

3 Wall deformation model

The aim of this paper is to study influence of stenotic regions in blood vessels. In order to model biological structure several models have been proposed in literature. For example, to model flow in a collapsible tubes a two-dimensional thin shell model can be used, see results of Wall et al. [9] on flow-thinwalled problems and FSI methods. Recently Čanič et al. [4] developed a new one-dimensional model for arterial walls, the linearly viscoelastic cylindrical Koiter shell model, that is closed and rigorously derived by energy estimates, asymptotic analysis and homogenization techniques. The viscous fluid dissipation imparts long-term viscoelastic memory effects represented by higher order derivatives.

In the present paper we will consider the *generalized string model* for vessel wall deformation [20]. The model derived in [20] is valid only for straight tubes with constant reference radius R_0. In order to model stenotic occlusion we want to extend this model by assuming that the arterial reference radius at rest R_0 is not constant but a function of an actual position.

Let us consider a 3D radially symmetric tube, see Fig. 2. We assume to have deformations only in the radial direction and set $x_1 = z$-direction and $x_2 = r$-radial direction. The radial wall displacement, constant with respect to the angle θ, is defined as

$$\eta(z, t) = R(z, t) - R_0(z),$$

where $R(z, t)$ is the actual radius and $R_0(z)$ is the reference radius at rest. Since the actual radius of the compliant tube is given by $R(z, t) = R_0(z) + \eta(z, t)$, the reference radius R_0 and the actual radius R coincides for fixed solid tube and are dependent only on spatial variable z. The assumption of radial geometry allow us to approximate the length of arc $dc \approx Rd\theta$, $dc \approx R_0 d\theta$, see Fig. 2 and also [20]. We assume also the small deformation gradient of displacement ($\partial_z \eta$, $\partial_\theta \eta$), which implies the linear constitutive law (linear elasticity) of the vessel wall. The wall thickness is assumed to be small and constant. Moreover we approximate the infinitesimal surface in the following way $S \approx dc\, dl$.

The linear momentum law $Force = mass \times acceleration$ is applied in the radial direction to obtain the equation for η.

$$mass = \rho_w \hbar\, dc\, dl, \qquad acceleration = \frac{\partial^2 R(z, t)}{\partial t^2} = \frac{\partial^2 \eta(z, t)}{\partial t^2}, \tag{7}$$

where ρ_w is the density of the wall and $\hbar$ its thickness.

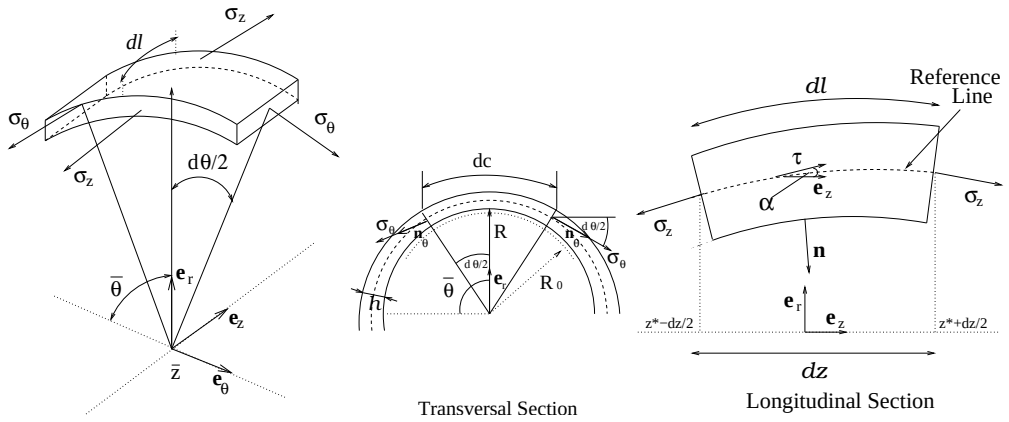

Figure 2: Small portion of vessel wall with physical characteristics, see also [20]

Now we evaluate forces acting on the vessel wall. The tissue surrounding the vessel wall interacts with the vessel wall by exerting a constant pressure P_w. The resulting tissue force is $\boldsymbol{f}_{tissue} = -P_w \boldsymbol{n}\, dc\, dl \approx -P_w \boldsymbol{n} R d\theta\, dl$.

The forces from the fluid on Γ^w are represented by the normal component of the Cauchy stress tensor $\boldsymbol{f}_{fluid} = -\mathbf{T}_f\, \boldsymbol{n}\, dc\, dl$. By summing the tissue and fluid forces we get the resulting external force acting on the vessel wall along the radial direction ($\boldsymbol{f}_{ext} = \boldsymbol{f}_{tissue} + \boldsymbol{f}_{fluid}$):

$$\begin{aligned} f_{ext}\Big|_{\Gamma_0^w} &= \boldsymbol{f}_{ext} \cdot \boldsymbol{e}_r \approx (-\mathbf{T}_f - P_w \mathbf{I})\boldsymbol{n} \cdot \boldsymbol{e}_r \frac{R}{R_0} \frac{\sqrt{1+(\partial_z R)^2}}{\sqrt{1+(\partial_z R_0)^2}}\, dc\, dl \\ &\approx -(\mathbf{T}_f + P_w \mathbf{I})\boldsymbol{n} \cdot \boldsymbol{e}_r \frac{R}{R_0}\, dc\, dl \approx -(\mathbf{T}_f + P_w \mathbf{I})\boldsymbol{n} \cdot \boldsymbol{e}_r R\, d\theta\, dl, \end{aligned}$$

where $\boldsymbol{n} = \frac{1}{\sqrt{1+(\partial_z R)^2}}(-\partial_z R, 1)$ is the unit outward normal to the boundary Γ^w. The term

$$\frac{R\sqrt{1+(\partial_z R)^2}}{R_0\sqrt{1+(\partial_z R_0)^2}}$$

arrives from the transformation to the Lagranian coordinates, in particular we have the transformation of the curve $\Gamma^w := \{(z, R(z)), z \in (-L, L)\}$ to the curve $\Gamma_0^w := \{(z, R_0(z)), z \in (-L, L)\}$, see also [8] for more details. Due to the assumption on smallness of $\partial_z \eta$ we get the final expression.

The internal forces acting on the vessel portion are due to the circumferential stress $\boldsymbol{\sigma}_\theta$ (constant with respect to the angle) and the longitudinal stress $\boldsymbol{\sigma}_z$. Both stresses are directed along the normal to the surface to which they act. Let us denote $\sigma_\theta = \boldsymbol{\sigma}_\theta \cdot \boldsymbol{n}$. Further the longitudal stress $\boldsymbol{\sigma}_z$ is parallel to tangent, i.e. $\boldsymbol{\sigma}_z = \pm\sigma_z \boldsymbol{\tau}$, where the sign is positive if the versus of the normal to the surface on which $\boldsymbol{\sigma}_z$ is acting is the same as those chosen for $\boldsymbol{\tau}$.

We have $f_{int} = (\boldsymbol{f}_\theta + \boldsymbol{f}_z)\cdot \boldsymbol{e}_r$ and

$$\begin{aligned}
\boldsymbol{f}_\theta \cdot \boldsymbol{e}_r &= \Big[\boldsymbol{\sigma}_\theta\Big(\bar\theta + \frac{d\theta}{2}\Big) + \boldsymbol{\sigma}_\theta\Big(\bar\theta - \frac{d\theta}{2}\Big)\Big]\cdot \boldsymbol{e}_r \hbar\, dl = 2|\sigma_\theta| cos\Big(\frac{\pi}{2} + \frac{d\theta}{2}\Big)\hbar\, dl \\
&= -2|\sigma_\theta| \sin\left(\frac{d\theta}{2}\right)\hbar\, dl \approx -|\sigma_\theta|\hbar\ d\theta\, dl = -E\frac{\eta}{R_0}\hbar\ d\theta\, dl, \\
\boldsymbol{f}_z \cdot \boldsymbol{e}_r &= \Big[\boldsymbol{\sigma}_z\Big(z^* + \frac{dz}{2}\Big) + \boldsymbol{\sigma}_z\Big(z^* - \frac{dz}{2}\Big)\Big]\cdot \boldsymbol{e}_r \hbar\, dc \\
&= \frac{\boldsymbol{\tau}(z^* + \frac{dz}{2}) - \boldsymbol{\tau}(z^* - \frac{dz}{2})}{dz}\cdot \boldsymbol{e}_r \hbar|\sigma_z|\, dz\, dc \\
&\approx |\sigma_z|\Big[\frac{d\boldsymbol{\tau}}{dz}(z^*)\Big]\cdot \boldsymbol{e}_r \hbar\, dz\, dc \\
&\approx \left(\frac{\partial^2\eta}{\partial z^2} + \frac{\partial^2 R_0}{\partial z^2}\right)\left[1 + \left(\frac{\partial R_0}{\partial z}\right)^2\right]^{-1} \boldsymbol{n}\cdot \boldsymbol{e}_r|\sigma_z|\hbar dz\, dc.
\end{aligned}$$

Here we have used the following properties. According to the linear elasticity assumption the stress tensor $\boldsymbol{\sigma}_\theta$ is proportional to the relative circumferential prolongation, i.e.

$$\boldsymbol{\sigma}_\theta = E\frac{2\pi(R - R_0)}{2\pi R_0} = E\frac{\eta}{R_0}, \quad E \text{ is Young's modulus of elasticity.}$$

To evaluate the longitudinal force we have used the following result, that is a generalization of Lemma C.1 in [20].

Lemma. *If $\frac{\partial\eta}{\partial z}$ is small then*

$$\frac{d\boldsymbol{\tau}}{dz}(z^*) \approx \left(\frac{\partial^2\eta}{\partial z^2} + \frac{\partial^2 R_0}{\partial z^2}\right)\left[1 + \left(\frac{\partial R_0}{\partial z}\right)^2\right]^{-1}\boldsymbol{n}.$$

Proof: Let a parametric curve $\mathbf{c}$ be defined at each t on the plane (z, r) by

$$\mathbf{c} : \mathbb{R} \to \mathbb{R}^2,\ z \to (c_1(z), c_2(z)) = (z, R(z,t)) = (z, R_0(z,t) + \eta(z,t)),$$

and $\boldsymbol{\tau}$, $\boldsymbol{n}$, κ denote the tangent, the normal and the curvature of $\mathbf{c}$, respectively. Then according to the Serret-Frenet formula [20] we have

$$\frac{d\tau}{dz}(z) = \left|\frac{d\mathbf{c}}{dz}(z)\right|\kappa(z)\tilde{\boldsymbol{n}}(z).$$

Here $\tilde{\boldsymbol{n}} = \pm\boldsymbol{n}$ is the normal oriented towards the center of curvature. Furthermore since we assume $\frac{\partial\eta}{\partial z}$ small, we have

$$\begin{aligned}
\left|\frac{d\mathbf{c}}{dz}(z)\right| &= \left[1 + \left(\frac{\partial R}{\partial z}\right)^2\right]^{1/2} \approx \left[1 + \left(\frac{\partial R_0}{\partial z}\right)^2\right]^{1/2} \quad \text{and} \\
\kappa &= \left|\frac{dc_1}{dz}\frac{d^2c_2}{dz^2} - \frac{dc_2}{dz}\frac{d^2c_1}{dz^2}\right|\left|\frac{d\mathbf{c}}{dz}\right|^{-3} = \left|\frac{\partial^2 R}{\partial z^2}\right|\left[1 + \left(\frac{\partial R}{\partial z}\right)^2\right]^{-\frac{3}{2}} \\
&\approx \left|\frac{\partial^2 R_0 + \partial^2\eta}{\partial z^2}\right|\left[1 + \left(\frac{\partial R_0}{\partial z}\right)^2\right]^{-\frac{3}{2}}.
\end{aligned}$$

Since the sign of $\frac{\partial^2 R}{\partial z^2}$ determines the convexity of curve, $\tilde{\boldsymbol{n}} = sign\left(\frac{\partial^2 R}{\partial z^2}\right)\boldsymbol{n}$, we obtain the desired result. ■

By summing up all contribution of balancing forces we have from the linear momentum law

$$\left\{ \rho_w \hbar R \frac{\partial^2 \eta}{\partial t^2} - |\sigma_z| \frac{\left(\frac{\partial^2 \eta}{\partial z^2} + \frac{\partial^2 R_0}{\partial z^2}\right)}{\left[1 + \left(\frac{\partial R_0}{\partial z}\right)^2\right]} \boldsymbol{n} \cdot \boldsymbol{e}_r R \hbar \frac{dz}{dl} + \frac{E\hbar\eta}{R_0} + (\mathbf{T}_f + P_w \mathbf{I})\boldsymbol{n} \cdot \boldsymbol{e}_r R \right\} d\theta\, dl = \mathcal{O}(d\theta dl).$$

Note that $\boldsymbol{n} \cdot \boldsymbol{e}_r = 1/\sqrt{1 + (\partial_z R)^2} \approx 1/\sqrt{1 + (\partial_z R_0)^2}$ and

$$\frac{dz}{dl} \approx \cos(\measuredangle(\boldsymbol{e}_z, \boldsymbol{\tau})) = \boldsymbol{e}_z \cdot \boldsymbol{\tau} \approx 1/\sqrt{1 + (\partial_z R_0)^2},$$

see Fig. 2. Thus by dividing the former equation by $\rho_w \hbar\, R\, d\theta\, dl$ and passing to the limit for $d\theta \to 0$, $dl \to 0$ we obtain the so called *vibrating string model*. By adding the damping term $-c\partial^3_{tzz}\eta$, $c > 0$ at the left hand side we get the *generalized string model* for cylindrical geometry with a non-constant reference radius $R_0(z)$

$$\frac{\partial^2 \eta}{\partial t^2} - \frac{|\sigma_z|}{\rho_w} \frac{\left(\frac{\partial^2 \eta}{\partial z^2} + \frac{\partial^2 R_0}{\partial z^2}\right)}{\left[1 + \left(\frac{\partial R_0}{\partial z}\right)^2\right]^2} + \frac{E\eta}{\rho_w R_0 R} - c\frac{\partial^3 \eta}{\partial t \partial^2 z} = -\frac{(\mathbf{T}_f + P_w \mathbf{I})\boldsymbol{n} \cdot \boldsymbol{e}_r}{\rho_w \hbar} \frac{R}{R_0}. \tag{8}$$

4 Remark on theoretical results

For the above problem on shear-dependent fluid flow in deforming domain we have proved the existence and uniqueness of weak solution, see [14], see also [31], [7] for results on Newtonian fluid. The existence and uniqueness for 2D computational domain $\Omega(h) = \{(x_1, x_2, t) : 0 < x_1 < L,\ 0 < x_2 < h(x_1, t)\}$ is proven, where an a-priori known domain deformation function $h = h(x_1, t)$ is considered, i e. existence for solution for one global iteration with respect to the domain (explained in Section 5.1) has been proved. The finalization of this proof for $\Omega(\eta)$, done due limiting process of $h - R_0 = \eta^{(k)} \to \eta$ for $k \to \infty$ is shown using fixed point theorem for a special case of deformation equation and for a pseudo-compressible and κ-approximated system (1), (2), (8). See [7, Section 2] for details on $\kappa-$ approximation of the interface condition (2)-(8).

In what follows we introduce the main theoretical result given in [14]. We define space

$$\begin{aligned} \boldsymbol{V} &\equiv \left\{ \boldsymbol{w} \in W^{1,p}(D)^2 :\ w_1 = 0 \ \text{ on } S_w \text{ and } w_2 = 0 \ \text{ on } S_{in} \cup S_{out} \cup S_c \right\}, \\ S_w &= \{(y_1, 1) : 0 < y_1 < L\}, \\ S_{in} &= \{(0, y_2) : 0 < y_2 < 1\}, \\ S_{out} &= \{(L, y_2) : 0 < y_2 < 1\}, \\ S_c &= \{(y_1, 0) : 0 < y_1 < L\}, \end{aligned} \tag{9}$$

where $\mathbf{y} \in D = \{(y_1, y_2);\ 0 < y_1 < L,\ 0 < y_2 < 1\}$, $0 < t < T$ is a fixed rectangle computational domain (moving domain $\Omega(h)$ has been transformed to the rectangle D).

For viscous shear dependent tensor $\tau = \mu(|D(\nabla \boldsymbol{u})|)D(\nabla \boldsymbol{u})$ we assume that there exist a potential $\mathcal{U} \in C^2(\mathbb{R}^{2\times 2})$ of τ, such that for some $1 < p < \infty$ (we remind that $\frac{p-2}{2} = q$), $C_1,\ C_2 > 0$, we have for all $\eta,\ \xi \in \mathbb{R}^{2\times 2}_{sym}$ and $i,\ j,\ k,\ l = 1, 2$,

$$\frac{\partial \mathcal{U}(\eta)}{\partial \eta_{ij}} = \tau_{ij}(\eta) \tag{10}$$

$$\mathcal{U}(\mathbf{0}) = \frac{\partial \mathcal{U}(\mathbf{0})}{\partial \eta_{ij}} = 0 \tag{11}$$

$$\frac{\partial^2 \mathcal{U}(\eta)}{\partial \eta_{mn} \partial \eta_{rs}} \xi_{mn} \xi_{rs} \geq C_1\ (1 + |\eta|)^{p-2} |\xi|^2 \tag{12}$$

$$\left| \frac{\partial^2 \mathcal{U}(\eta)}{\partial \eta_{ij} \partial \eta_{kl}} \right| \leq C_2 (1 + |\eta|)^{p-2}. \tag{13}$$

We denote by $(\tilde{\boldsymbol{u}}, \tilde{\eta}_t) \in D$ the solution in a transformed domain D, i.e.,

$$\begin{aligned} \tilde{\boldsymbol{u}}(y_1, y_2, t) &= \boldsymbol{u}(y_1, h(y_1, t), t), \\ \tilde{p}(y_1, y_2, t) &= \rho^{-1} p(y_1, h(y_1, t), t), \quad \mathbf{y} \in D, \end{aligned}$$

as well as the boundary data

$$\begin{aligned} \tilde{P}_{in}(y_2, t) &= \rho^{-1} P_{in}(y_2 h(0, t), t), \quad y_2 \in (0, 1) \\ \tilde{P}_{out}(y_2, t) &= \rho^{-1} P_{out}(y_2 h(L, t), t), \quad y_2 \in (0, 1) \\ \tilde{P}_w(y_1, t) &= \rho^{-1} P_w(h(y_1, t), t), \quad y_1 \in (0, L). \end{aligned}$$

Neumann outflow and inflow boundary condition with dynamical pressures $P_{in/out} - \frac{\rho}{2}|u_1|^2$ on the right hand side have been considered for horizontal velocities, vertical velocities have been set to zero.

Moreover, for a priori known deformation $h = R_0 + \eta^k$ we assume

$$0 < \alpha \leq h(x_1, t) \leq \alpha^{-1}\ , \tag{14}$$

$$\left| \frac{\partial h^i}{\partial x_1}(x_1) \right| + \left| \frac{h^i(x_1) - h^{i-1}(x_1)}{\Delta t} \right| \leq K \tag{15}$$

$$h(0, t) = R_0(0), \quad h(L, t) = R_0(L), \quad h(x_1, 0) = R_0(x_1) > 0.$$

We proved the following existence result for some shear thinning and shear thickening fluids.

Theorem 4.1 (Existence of weak solution)**.** *[14]*
Let $p \geq (1 + \sqrt{5})/2$. Assume that $h \in W^{1,\infty}((0, T) \times (0, L))$ satisfies (14), (15) and that the boundary data $\tilde{P}_{in}, \tilde{P}_{out} \in L^\infty(0, T; L^2(0, 1))$, $\tilde{P}_w \in L^\infty(0, T; L^2(0, L))$. Furthermore, assume that the properties (10)–(13) for the viscous stress tensor hold.

Then there exist a weak solution $(\boldsymbol{u}, \eta)$ of the problem (1), (2), (8) such that
i) $(\tilde{\boldsymbol{u}}, \tilde{\eta}_t) \in [L^p(0, T; \boldsymbol{V}) \times L^\infty(0, T; H_0^1(0, L))] \cap [L^\infty(0, T; L^2(D)) \times H^1(0, T; L^2(0, L))]$,

ii) $\boldsymbol{u}$ *satisfies the divergence free condition div* $\boldsymbol{u} = 0$ *a.e on* $\Omega(h)$ *and the following integral identity holds*

$$\begin{aligned}
&\int_{\Omega(h)} \left\{ -\rho \boldsymbol{u} \cdot \frac{\partial \varphi}{\partial t} + 2\mu(|D(\boldsymbol{u})|)D(\boldsymbol{u})D(\varphi) + \rho \sum_{i,j=1}^{2} u_i \frac{\partial u_j}{\partial x_i} \varphi_j \right\} dxdt \\
&+ \int_0^T \int_{\Gamma_{out}} \left(P_{out} - \frac{\rho}{2} |u_1|^2 \right) \varphi_1(L, x_2, t)\, dSdt \\
&- \int_0^T \int_{\Gamma_{in}} \left(P_{in} - \frac{\rho}{2} |u_1|^2 \right) \varphi_1(0, x_2, t)\, dSdt \\
&+ \int_0^T \int_{\Gamma_w} \left(P_w - \frac{\rho}{2} u_2 \left(u_2 - \frac{\partial h}{\partial t} \right) \right) \varphi_2(x_1, h(x_1, t), t)\, dSdt \\
&+ \int_0^T \int_0^L \left(-\frac{\partial \eta}{\partial t} \frac{\partial \xi}{\partial t} + c \frac{\partial^2 \eta}{\partial x_1 \partial t} \frac{\partial \xi}{\partial x_1} + a \frac{\partial \eta}{\partial x_1} \frac{\partial \xi}{\partial x_1} - a \frac{\partial^2 R_0}{\partial x_1^2} \xi + b\eta\, \xi \right) (x_1, t)\, dx_1 dt \;=\; 0
\end{aligned}$$

for every test functions

$$\begin{aligned}
&\varphi = (x_1, x_2, t) = \tilde{\varphi}\left(x_1, \frac{x_2}{h(x_1, t)}, t \right), \quad \tilde{\varphi} \in L^p(0, T; \boldsymbol{V}) \cap H^1(0, T; L^2(D)), \\
&\qquad\qquad \textit{such that div } \varphi = 0 \quad \textit{a.e on } \Omega(h), \\
&\xi(x_1, t) = \tilde{\varphi}_2(x_1, 1, t)\rho_w \hbar; \quad \xi(0, \cdot) = \xi(L, \cdot) = 0
\end{aligned}$$

In this result the structure equation is fulfilled in a slightly modified sense

$$\begin{aligned}
&\frac{\partial^2 \eta}{\partial t^2} - a \frac{\partial^2 \eta}{\partial x_1^2} + b\eta - c \frac{\partial^3 \eta}{\partial t \partial x_1^2} = \\
&-\frac{R}{R_0} \frac{\mathbf{T}_f \boldsymbol{n} \cdot \boldsymbol{e}_r}{\rho_w \hbar} - \frac{R}{R_0} \frac{P_w \mathbf{I} \boldsymbol{n} \cdot \boldsymbol{e}_r}{\rho_w \hbar} + \frac{\rho}{2} \frac{u_2(u_2 - \partial_t h)}{\rho_w \hbar} + a \frac{\partial^2 R_0}{\partial x_1^2} \\
&\qquad\qquad\qquad\qquad\qquad\qquad\qquad\qquad \text{a.e. on } [0, L] \times (0, T).
\end{aligned}$$

Furthermore, the interface boundary condition

$$u_2(x_1, h(x_1, t), t) = \frac{\partial \eta}{\partial t}(x_1, t)$$

holds a.e. at the moving wall Γ^w. The additional term $\frac{\rho}{2} u_2(u_2 - \partial_t h)$ on the right hand side of deformation equation disappears if $h \to R_0 + \eta$.

The proof of existence and uniqueness is based on energy method, a-priori estimates, compact imbeddings and theory of monotone operators in order to take into account growth character of viscous non-linear stress $\tau(D)$. The uniqueness and continuous dependence of weak solution on data h, $\tilde{P}_{in}$, $\tilde{P}_{out}, \tilde{P}_w$ are essential for proving the contractiveness of domain iterations, see [7, Section 10] for details. For related results on shear dependent fluid or fluid-structure interaction problems see also [18], [11], [5], [26], [28].

5 Numerical methods

5.1 Decoupling method for fluid-structure interaction: the global iterative method

The coupling between the fluid and the domain is twofold. First, the stress tensor of the fluid influences the domain deformation since it appears on the right-hand side of the structure equation (8). On the other hand, the Dirichlet boundary condition (2) on Γ^w is related to the domain deformation η.

The fluid-structure interaction given by conditions (2) and (8) is decoupled by a *global iteration with respect to the domain geometry*. It means that in the k-th iteration, the vector $(\boldsymbol{u}^k, p^k, \eta^k)$ is obtained as a solution of (1) for all $(x,t) \in \Omega(\eta^{(k-1)})$, and (8) for all $x_1 \in (-L, L)$. Instead of condition (2) we use

$$u_2(x_1, x_2, t) = \frac{\partial \eta^{k-1}(x_1,t)}{\partial t} = u_2^{grid}(x_1, x_2, t),\ u_1(x_1,t) = 0, \qquad \text{on } \Gamma^{w,k-1}, \tag{16}$$

where $\Gamma^{w,k-1} = \{(x_1, x_2);\ x_2 = R_0(x_1) + \eta^{k-1}(x_1,t),\ x_1 \in (-L,L)\}$ and $\boldsymbol{u}^{grid}$ is the velocity of mesh movement related to smoothing the grid after moving its boundary (we allow just movement in the x_2 direction, x_1 direction is neglected), see also [31].

Further we linearize the equation (8) replacing the non-linear term on its left hand side by $E\eta/(\rho_w(R_0 + \eta^{k-1})R_0)$. In order to decouple (1) and (8) we evaluate the forcing term at the right hand side of (8) at the old time step t^{n-1}, see also Fig 4. Convergence of this global method was verified experimentally. Our extensive numerical experiences show fast convergence of domain deformation, two iteration of domain deformation differ about $10^{-4}cm$ (for e.g., $R_0 = 1cm$) pointwisely after few, about 5 iterations. As an example we have depicted in Figure 3 a deformed vessel wall after 1, 2, 3 and 4 global iterations at the same time $T = 0.36s$. It illustrates that the vessel wall converges to one curve and does not change significantly already after second iteration, see Fig. 3. For theoretical proof of the convergence $\eta^k \to \eta$ see Section 4 and [14].

5.2 Discretization methods

For the numerical approximation of (1), (2) and (8) we have used as a basic software the UG software toolbox [1] and extended it by adding the shear-dependent viscosity as well as by adding the solver for the wall deformation equation (8). In UG the problem class library for the Navier-Stokes equations in moving domain is based on the ALE formulation, see [3]. The spatial discretization of the fluid equations (1) is realized by the finite volume method with the pseudo-compressibility stabilization. This stabilization results in the elliptic equation for the pressure. The non-linear convective term is linearized by the Newton or fixed point method, see e.g., [17].

We describe our approximation methods in what follows.

Linearization of the viscous term: According to Taylor's expansion we have

$$\begin{aligned} \mu(|D(\nabla \boldsymbol{u})|)D(\nabla \boldsymbol{u}) &= \mu(|D(\nabla \boldsymbol{u}^{old})|)D(\nabla \boldsymbol{u}^{old}) \\ &+ \frac{d\left[\mu(|D(\nabla \boldsymbol{u})|)D(\nabla \boldsymbol{u})\right]}{d(\nabla \boldsymbol{u})}(\nabla \boldsymbol{u}^{old})(\nabla \boldsymbol{u} - \nabla \boldsymbol{u}^{old}) + \mathcal{O}((\nabla \boldsymbol{u} - \nabla \boldsymbol{u}^{old})^2), \end{aligned} \tag{17}$$

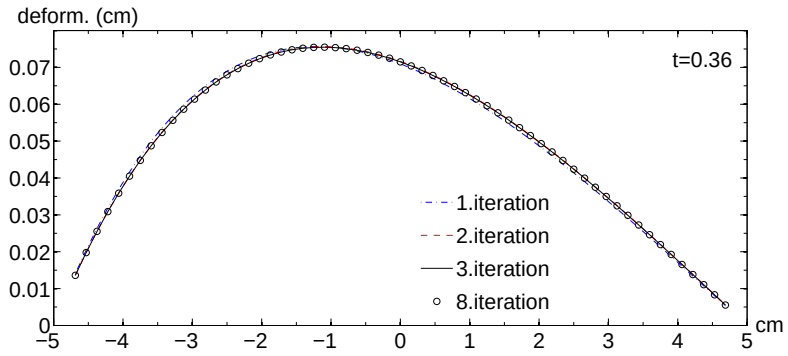

Figure 3: Wall deformation of a vessel at time $t = 0.36s$ at the 1., 2., 3., and 8. global iteration; after 2nd iteration curves coincide. Computed for the Carreau model with $Re = 40$, cf. (21)

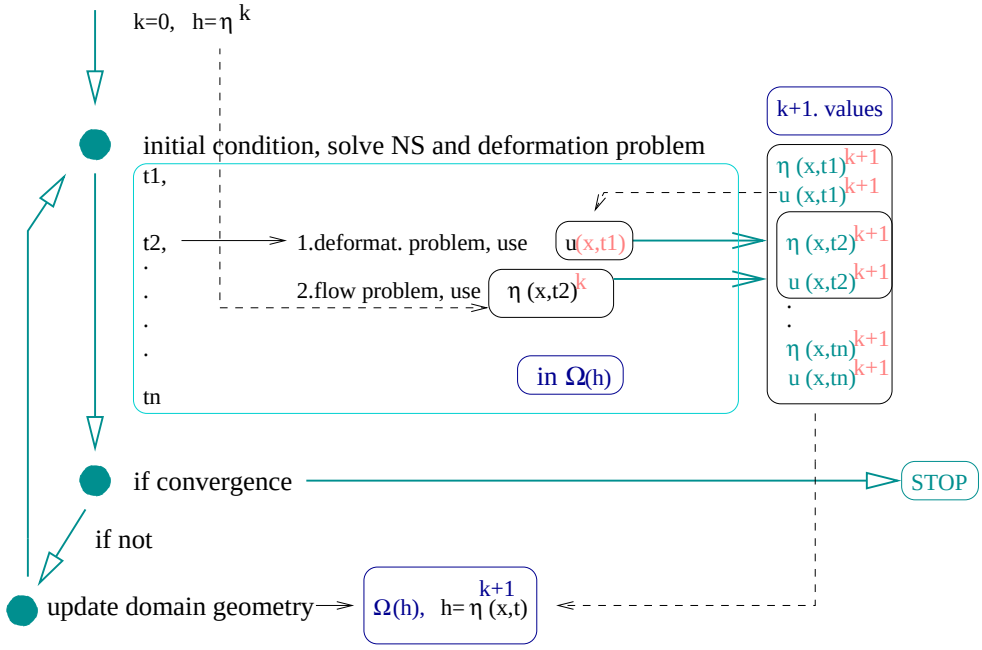

Figure 4: The sketch of the global iterative method

where

$$\frac{d\,[\mu(|D(\nabla \boldsymbol{u})|)D(\nabla \boldsymbol{u})]}{d(\nabla \boldsymbol{u})}(\nabla \boldsymbol{u}^{old}) = \mu(|D(\nabla \boldsymbol{u}^{old})|)\frac{1}{2}(I + I^T) + \frac{d\,\mu(|D(\nabla \boldsymbol{u})|)}{d\nabla \boldsymbol{u}}(\nabla \boldsymbol{u}^{old})D(\nabla \boldsymbol{u}^{old}).$$

Plugging the expression for $\frac{d[\mu(|D(\nabla \boldsymbol{u})|)\nabla \boldsymbol{u}]}{d(\nabla \boldsymbol{u})}$ into (17) and neglecting the higher order

term $\mathcal{O}((\nabla \boldsymbol{u} - \nabla \boldsymbol{u}^{old})^2)$ we obtain the Newton type iteration. By neglecting the term $\frac{d\,\mu(|D(\nabla \boldsymbol{u})|)}{d(\nabla \boldsymbol{u})}(\nabla \boldsymbol{u}^{old})D(\nabla \boldsymbol{u}^{old})$ - the second term from the above expression for derivative of $\mu(|D(\nabla \boldsymbol{u})|)D(\nabla \boldsymbol{u})$ we get the fixed point iterations

$$\mu(|D(\nabla \boldsymbol{u})|)D(\nabla \boldsymbol{u}) \approx \mu(|D(\nabla \boldsymbol{u}^{old})|)D(\nabla \boldsymbol{u}). \tag{18}$$

Here $(.)^{old}$ denotes the previous iteration.

In order to approximate the structure equation we apply the finite difference method. First we rewrite the second order equation (8) as a system of two first order equations. Set $\xi = \partial_t \eta$. Time discretization is realized by the following scheme

$$\begin{aligned} \frac{\xi^{n+1} - \xi^n}{\Delta t} - A\alpha \frac{\partial^2 \eta^{n+1}}{\partial x_1^2} &+ B\alpha \eta^{n+1} - C\alpha \frac{\partial^2 \xi^{n+1}}{\partial x_1^2} \\ &= H^n + A(1-\alpha)\frac{\partial^2 \eta^n}{\partial x_1^2} - B(1-\alpha)\eta^n + C(1-\alpha)\alpha \frac{\partial^2 \xi^n}{\partial x_1^2} \\ \frac{\eta^{n+1} - \eta^n}{\Delta t} &= \alpha \xi^{n+1} + (1-\alpha)\xi^n, \end{aligned}$$

where

$$A = \frac{|\sigma_z|}{\rho_w}\left[1 + \left(\frac{\partial R_0(x_1)}{\partial x_1}\right)^2\right]^{-2}, \qquad B = \frac{E}{\rho_w (R_0 + \eta) R_0} + \frac{(\mathbf{T}_f + P_w \mathbf{I})\boldsymbol{n} \cdot \boldsymbol{e}_r}{\rho_w \hbar R_0},$$

$$C > 0, \qquad H = \frac{|\sigma_z|}{\rho_w}\left(\frac{\partial^2 R_0(x_1)}{\partial x_1^2}\right)\left[1 + \left(\frac{\partial R_0(x_1)}{\partial x_1}\right)^2\right]^{-2} - \frac{(\mathbf{T}_f + P_w \mathbf{I})\boldsymbol{n} \cdot \boldsymbol{e}_r}{\rho_w \hbar}.$$

Physical meaning of quantities appearing in the coefficients A, B, C is following, see [8]: the Young modulus is $E = 0.75.10^5 dyn/cm^2$, the wall thickness $\hbar = 0.1cm$, the density of the vessel wall tissue $\rho_w = 1.1 g/cm^3$, $|\sigma_z| = G\kappa$, where $\kappa = 1$ is the Timoshenko shear correction factor and G is the shear modulus, $G = E/2(1+\sigma)$, where $\sigma = 1/2$ for incompressible materials. The coefficient $C = \gamma/(\rho_w \hbar)$, we have used $\gamma = 2.10^4$.

If $\alpha = 0$ we have an explicit scheme in time, for $\alpha = 1$ we obtain an implicit scheme. The parameter $\alpha = \frac{1}{2}$ yields the Newmark scheme, which is proven to be unconditionally stable at least in the case of homogeneous Dirichlet boundary conditions, see [19].

6 Numerical experiments

In this section we present a series of numerical experiments for fluid flow in a compliant vessel. The aim is to investigate differences in the behavior of Newtonian and non-Newtonian fluids in moving domains. We have chosen two non-Newtonian models for the blood flow often used in the literature, the Carreau and the Yeleswarapu model. Further, we study the influence of non-Newtonian rheology and of fluid-structure interaction on some hemodynamical wall parameters such as the wall shear stress WSS and the oscillatory shear index OSI.

We consider a two dimensional symmetric tube with a smooth stenosed region. Due to the symmetry we can restrict our computational domain to the upper half of the tube. A representative geometry is shown e.g. in Fig. 10. The impermeable moving wall Γ^w is modeled as a smooth stenosed constriction given as, see [16],

$$\begin{aligned} f(x_1) &= 1 - \frac{g}{2}\left(1 + \cos\left(\frac{\pi x_1}{2}\right)\right) \qquad \text{if } x_1 \in |r| \\ f(x_1) &= 1 \qquad\qquad\qquad\qquad\quad \text{if } x_1 \in (-L, -r) \cup (r, L). \end{aligned}$$

We took $L = 5$, $r = 2$, $g = 0.3$. These values give a stenosis with 30% area reduction which corresponds to a relatively mild occlusion, leading to local small increment of the Reynolds number.

Let $\Gamma^{in} = \{(-L, x_2);\, x_2 \in (0,1)\}$, $\Gamma^{out} = \{(L, x_2);\, x_2 \in (0,1)\}$, $\Gamma^s = \{(x_1, 0);\, x_1 \in (-L, L)\}$ denote the inflow, outflow and symmetry boundary, respectively. We prescribe the pulsatile parabolic velocity profile on the inflow boundary of the tube

$$u_1(-L, x_2) = V(R(t)^2 - x_2^2)f(t), \qquad u_2(-L, x_2) = 0, \tag{19}$$

where $R(t) = R_0(0) + \eta^k(0,t)$, $R_0(0) = 1$ and V is the maximal velocity at the inflow. For temporal function $f(t)$ modelling pulses of heart we have used two variants: $f(t) = sin^2(\pi t/\omega)$ with the period $\omega = 1s$ as well $f(t)$ arising from the iliac artery flow rate, see Fig.5. The flow rate is defined as

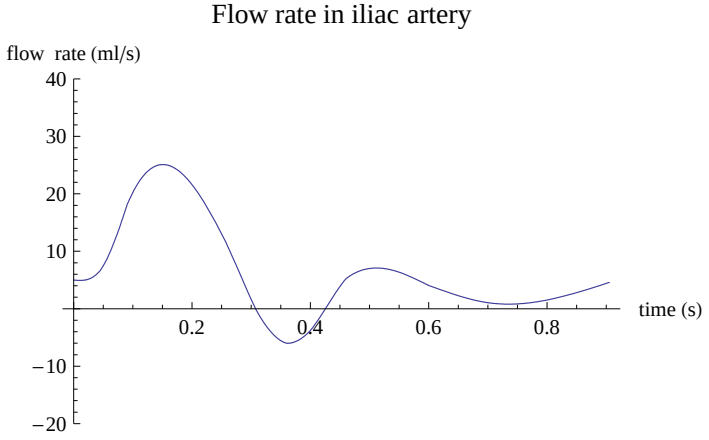

Figure 5: Flow rate $Q(t)$ in iliac artery, the period is $T = 0.9s$, (data obtained from [27] Fig. 3)

$$Q(t) = \int_{\Gamma^{in}} u_1 dx_2.$$

By integration inflow velocity (19) over Γ^{in} we obtain that $Q(t) = \frac{4}{3}V\pi R(t)^3 f(t)$. Consequently we get the relation for temporal function $f(t)$ in (19),

$$f(t) = Q(t)\frac{3}{4V\pi R(t)^3}. \tag{20}$$

For Γ^s the symmetry boundary condition $\partial_{x_2} u_1 = 0,\ u_2 = 0$ is prescribed and for Γ^{out} the Neumann type boundary condition $-\mathbf{T}_f \boldsymbol{n} = P_{out}\mathbf{I}\boldsymbol{n}$ is used. Since the viscosity of the non-Newtonian fluid is a function of shear rate, see Fig. 1, we compute the Reynolds number using averaged viscosity

$$Re = \frac{\rho V l}{\frac{1}{2}(\mu_0 + \mu_\infty)}, \tag{21}$$

where ρ is the fluid density, V is the characteristic velocity (maximal inflow velocity), l is the characteristic length (we take the diameter of the tube). In order to take into account also the effects of asymptotical viscosity values, we define $Re_0 = \rho V l/\mu_0,\ Re_\infty = \rho V l/\mu_\infty$ and introduce them in the Table 1 below as well.

In the following numerical experiments we have chosen in analogy to Nadau and Sequeira [16], $Re_0 = 30$ or $Re_0 = 60$ and $\mu_\infty = \frac{1}{2}\mu_0$ for the Carreau model (3) as well as for the Yeleswarapu model (4). We should point out that in [16] the authors studied similar problem, however they did not consider pulsatile flow and deforming vessel walls. They used however the generalized Oldroyd-B model for blood. In Section 6.2 we will also test the stability and robustness of the method for physiological parameters [29], see Table 1.

Table 1: Parameters for numerical experiments

$Re_0 = 30$	$Re_0 = 60$	$Re_0 = 30$	$Re_0 = 60$
Carreau model $q = 0,\ -0.322,\ -10$ $\lambda = 1$		**Yeleswarapu model** $\lambda = 14.81$	
$\mu_\infty = 1.26P$ $\mu_0 = 2.53P$ $V = 38\,cm/s$ $Re = 40$ $Re_\infty = 60$	$\mu_\infty = 0.63P$ $\mu_0 = 1.26P$ $V = 38\,cm/s$ $Re = 80$ $Re_\infty = 121$	$\mu_\infty = 1.26P$ $\mu_0 = 2.53P$ $V = 38\,cm/s$ $Re = 40$ $Re_\infty = 60$	$\mu_\infty = 0.63P$ $\mu_0 = 1.26P$ $V = 38\,cm/s$ $Re = 80$ $Re_\infty = 121$
physiological parameters $q = -0.322\ \ \lambda = 3.313$		physiological parameters	
	$\mu_\infty = 0.0345P$ $\mu_0 = 0.56P$ $V = 17cm/s$ $Re = 114$ $Re_\infty = 986$		$\mu_\infty = 0.05P$ $\mu_0 = 0.736P$ $V = 22.3cm/s$ $Re = 113$ $Re_\infty = 892$

6.1 Numerical experiments for model data

In what follows we plot the results comparing several aspects of Newtonian and non-Newtonian flow in the straight channel and in the channel with a stenotic occlusion. We chose the Dirichlet inflow boundary condition (19), which model some pulsatile parabolic velocity profile at the inflow. Here we took $f(t) = sin^2(\pi t/\omega)$, where $\omega = 1s$.

Fig. 6 describes time evolution of the wall deformation function η at two time instants $t = 0.36s$ and $t = 0.96s$ for the straight and stenotic compliant channel and for different non-Newtonian viscosities. Clearly, we can see effects due to the presence of stenosis in Fig. 6. The differences in wall deformation for non-Newtonian and Newtonian ($q = 0$) fluids are not significant. Fig. 7,8 describe the wall shear stress distribution (WSS) along the moving or fixed (solid) wall in the straight channel and in stenotic channel, respectively. We compare the WSS for the Newtonian and non-Newtonian fluids. Analogously as before we see that the WSS depends considerably on the geometry. In Fig. 8 peaks in the WSS due to the stenosis can be identified clearly for both Newtonian and non-Newtonian models. Fluid rheology is even more significant for WSS measurements; see different behaviour of WSS at $t = 0.36s$ in Fig. 7 and Fig. 8. Moreover, we can conclude that the WSS at $t = 0.36s$ is in general lower in compliant vessel than in solid one, see Fig. 7 for straight channel and Fig. 8 for stenotic situation.

Another important hemodynamic wall parameter is the oscillatory shear index OSI. Fig. 9 describes the behavior of the OSI in the straight and stenotic channel (both solid and compliant case). We can see new effects due to the presence of stenosis in the OSI. Moreover the peaks in the OSI are more dominant for the non-Newtonian models in comparison to the Newtonian flow. High OSI values indicate the areas with the large stenotic plug danger. Fig. 9 indicates, that such areas appear at the end of stenotic reduction. Numerical simulation with solid vessel walls indicates even higher oscillation of the wall shear stress. Thus, simulations without fluid-structure interaction would indicate more critical shear stress situation in vessels as they are actually present in elastic moving vessels.

We conclude this subsection with a statement, that the fluid rheology and domain geometry may have a considerable influence on the hemodynamic wall parameters WSS and OSI. The fluid-structure interaction aspect plays definitely significant role in the prediction of hemodynamical indices and should be involved in reliable computer simulations.

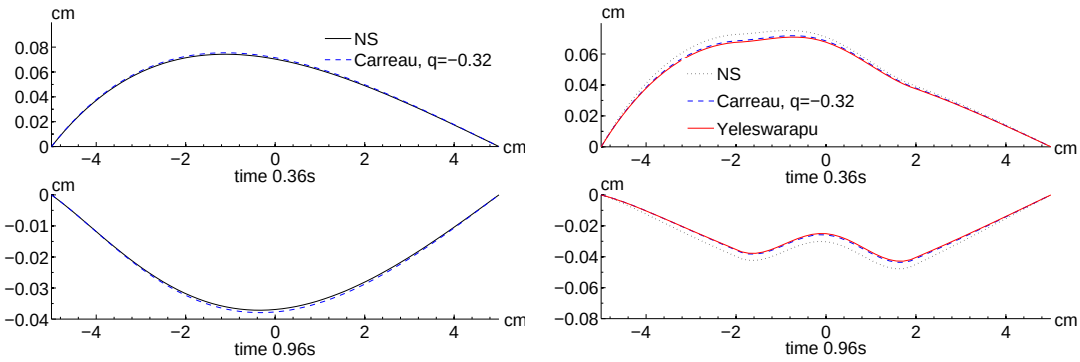

Figure 6: Deformation of the compliant vessel wall, left: the Newtonian (NS) and the Carreau models in the straight channel; right: the Newtonian (NS), the Yeleswarapu and the Carreau models in the stenosed channel, $Re = 40$

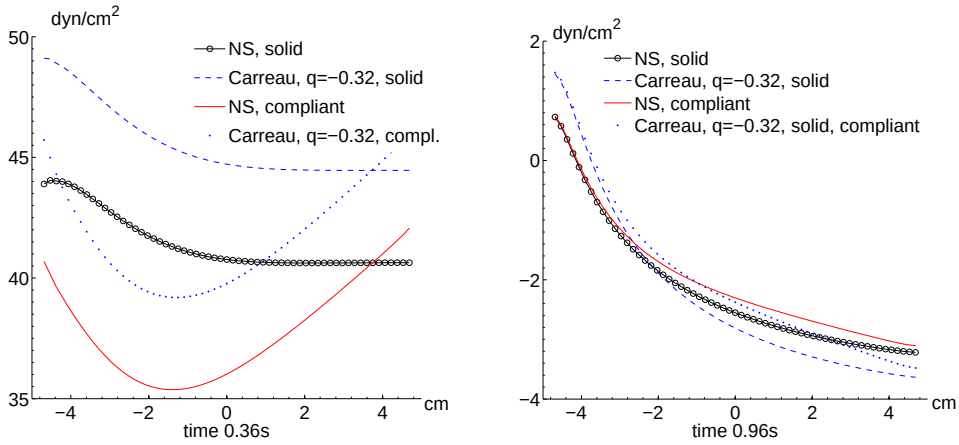

Figure 7: WSS along the straight vessel with solid as well as compliant walls, the Newtonian (NS) and the Carreau model, $Re = 40$, left: $t = 0.36s$, right: $t = 0.96s$

6.2 Numerical experiments for physiological parameters

We present several results comparing the behavior of both non-Newtonian models, the Carreau and the Yeleswarapu model with corresponding physiological parameters, see Table 1. In the first numerical experiment we consider the pulsatile velocity profile at the inflow as in Section 6.1.

Fig. 10 describes the velocity field at different times. We can clearly notice reversal flow areas due to pulsatile behavior of blood flow. In Fig. 11 the streamlines and the pressure distribution for the Yeleswarapu model at different time instants can be seen. Again at time $t = 0.96$, where the inflow velocity is decreasing we can observe reversal flow and vortices in the streamlines. Note also that some differences between the Carreau and the Yeleswarapu model have been observed in the wall deformation η, the OSI, as well as in the WSS, see Figs. 12, 13, respectively.

Further, our numerical experiments confirm, that the differences between Newtonian and non-Newtonian fluids in the wall deformation, wall shear stress and also OSI increase with increasing Reynolds numbers, see Figs. 14, 15 (left), 16.

In the next numerical experiment we consider the Neumann type boundary condition for deformation equation on the inflow boundary. This condition represents a free movement of vessel wall on the inflow and outflow part and seems to be more natural for modelling the flow in a part of elastic vessel. In this numerical experiment, moreover, we have introduced some damping of deformation in stenotic region. This is reasonable, since the stenotic occlusion is created by fat accumulated on the vessel wall and the stenotic plug may have different elastic properties. We considered Young's modulus E and damping parameter c in the structure equation (8) being following functions of longitudinal

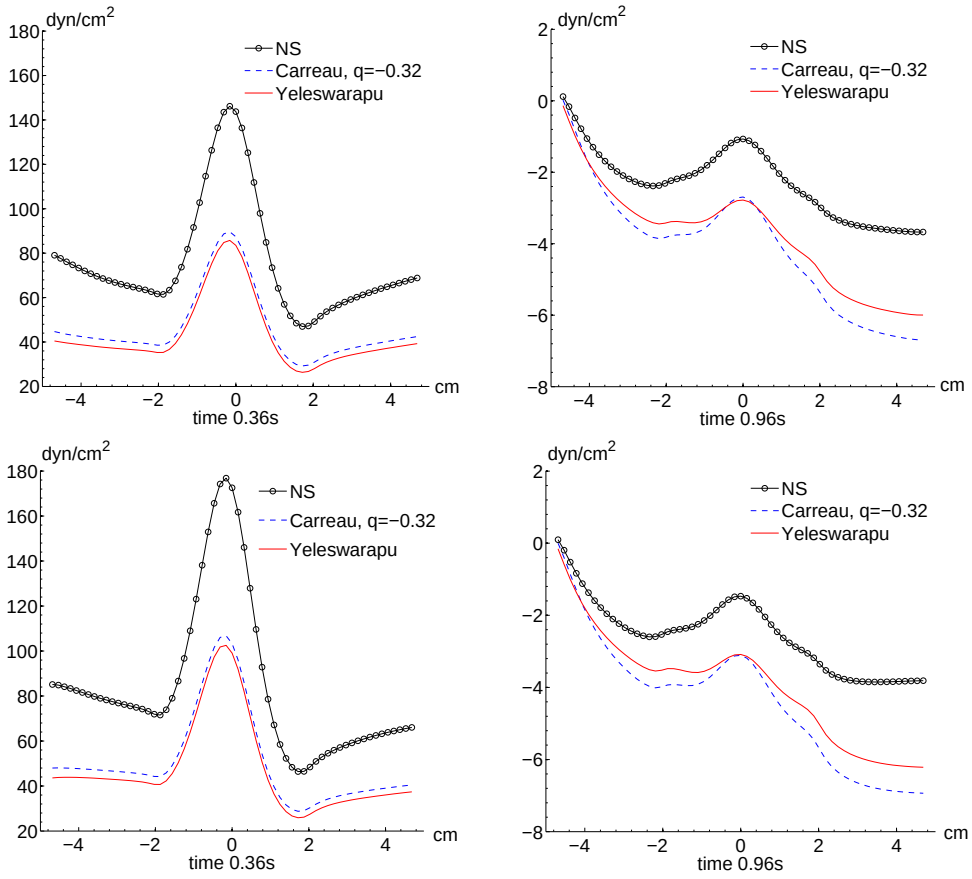

Figure 8: WSS along the vessel wall in stenosed compliant(top) and solid (bottom) channel, the Newtonian (NS), the Yeleswarapu and the Carreau models at two time instants, $Re = 40$

variable x

$$E = E(x) = \begin{cases} E & x \in (-5,-2) \cup (2,5) \\ E[1 + 0.1(x^2 - 4)] & x \in \langle -2, 2 \rangle, \end{cases}$$

$$c = c(x) = \begin{cases} 20.000 & x \in (-5,-2) \cup (2,5) \\ 20.000[1 - 0.01(x^2 - 4)] & x \in \langle -2, 2 \rangle. \end{cases}$$

In order to obtain more realistic hemodynamical situation, the parabolic velocity profile at the inflow was multiplied with temporal function derived from iliac artery measurements, see Fig. 5 and (20). We set the period $T = 0.9s$ and final computational time is chosen to be $t = 1.8s$. Numerical results are presented in Figs. 15 (right), 17, 18, 19.

Notice that the vessel wall at inflow and outflow are not fixed and the radius of vessel wall is increasing and decreasing according to the acting flow forces, Fig. 17. Due to

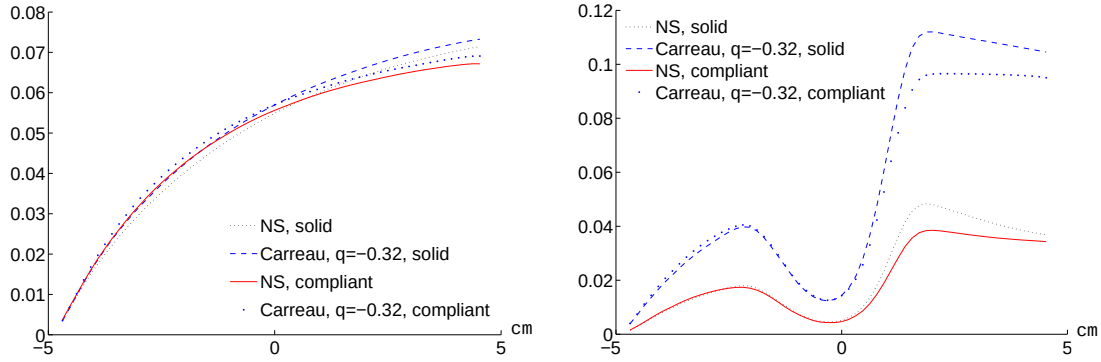

Figure 9: OSI indices along the compliant and the solid vessel wall computed for the Newtonian (NS) and the Carreau viscosity models with $q = -0.322$, the straight channel (left) and the stenosed channel (right), $Re = 40$

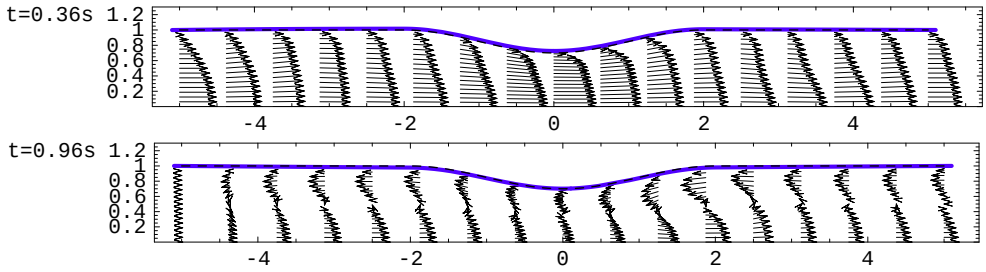

Figure 10: Numerical experiment using physiological parameters: the Carreau model, $Re = 80, t = 0.36s$ (top) and $t = 0.96s$ (bottom), velocity field

the increased damping parameter and decreased elasticity in the stenosed area the wall deformation presented in Fig. 17 is reduced considerably in comparison to the previous experiments, e.g. Fig. 14. Effects of different elasticity behavior at the stenosed part have also considerable influence on the behavior of hemodynamical wall parameters OSI and WSS, see Figs. 15, 18. Comparing pictures for streamlines as well as pressure presented in Fig. 19 we can notice much more complex phenomena, different types of recirculation zones as well as flow patterns.

$t = 0.36s$

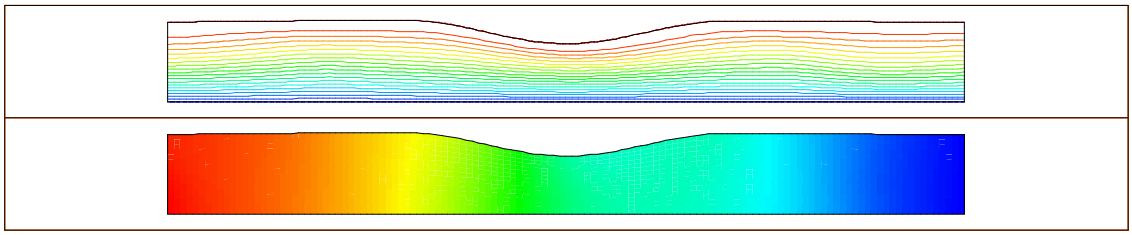

$t = 0.96s$

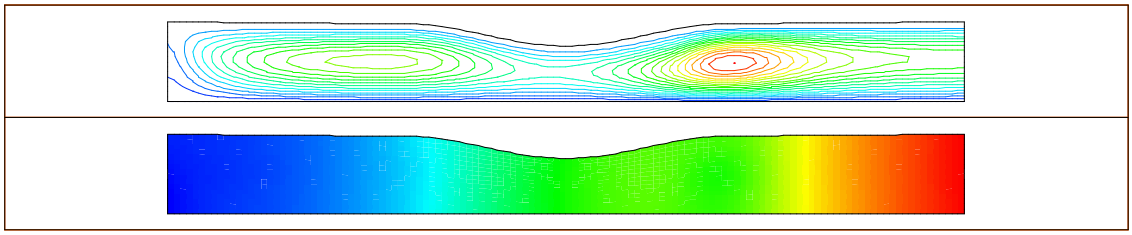

Figure 11: Numerical experiment using physiological parameters: the streamlines and the pressure distribution for the Yeleswarapu model at two time instants, $t = 0.36s$ (top) and $t = 0.96$ (bottom), $Re = 80$

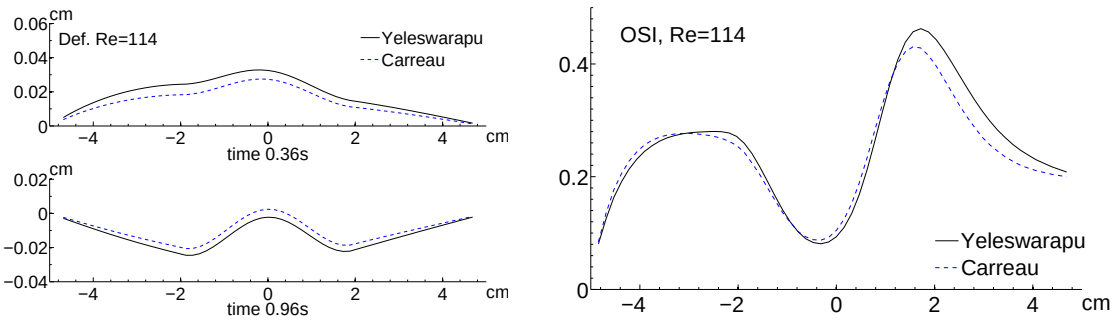

Figure 12: Numerical experiment in stenosed vessel using physiological parameters, left: wall deformation at two time instants, right: OSI indices

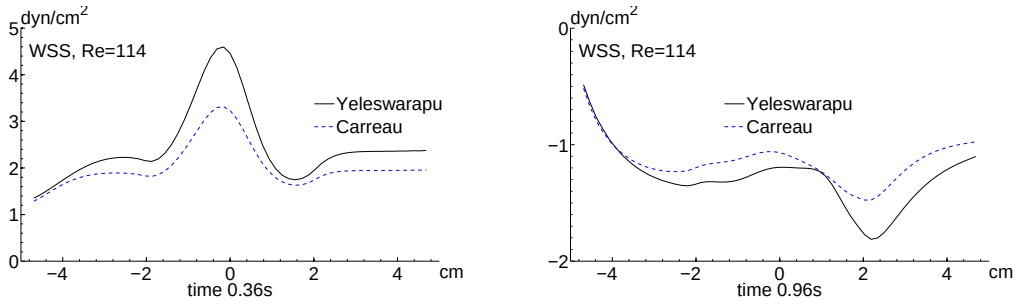

Figure 13: Numerical experiment using physiological parameters, comparison of the WSS for non-Newtonian models at two time instants $t = 0.36s$, $t = 0.96s$

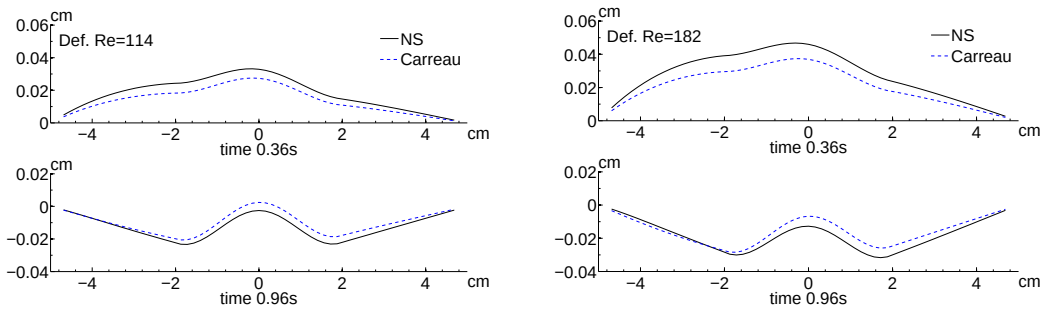

Figure 14: Numerical experiment using physiological parameters: comparison of wall deformations for different Reynolds numbers, left: Re=114, right: Re=182, at two time instants $t = 0.36s$, $t = 0.96s$

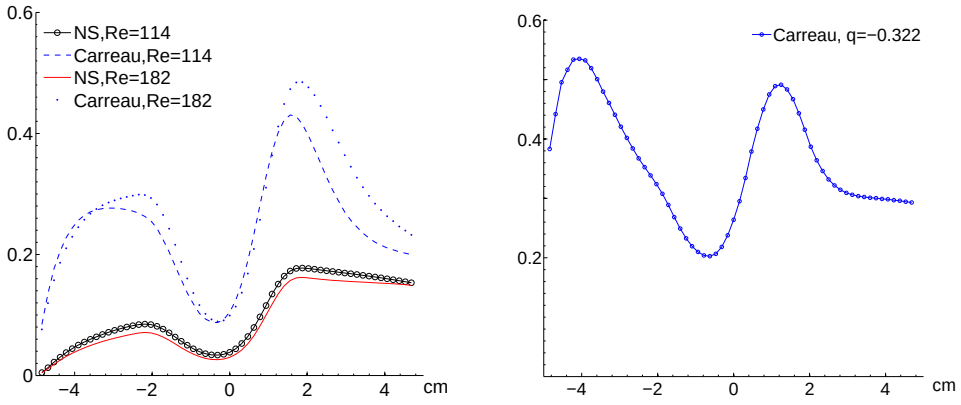

Figure 15: Numerical experiment using physiological parameters: left: the OSI indices for different Reynolds numbers, right: OSI index for iliac artery inflow, Neumann boundary condition for η and damping of deformation in stenotic region

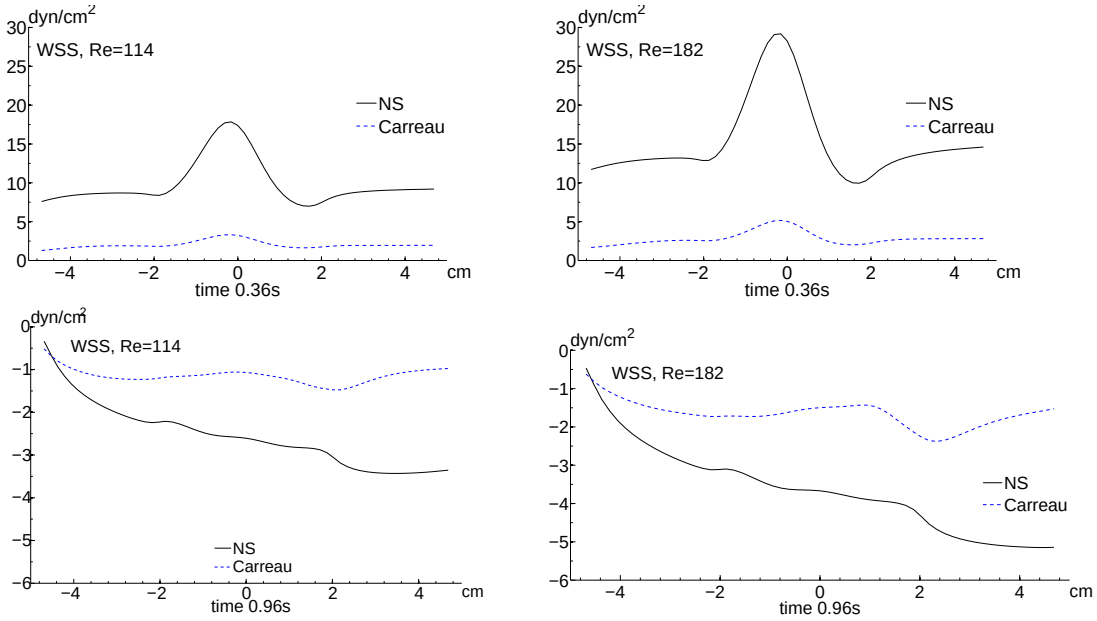

Figure 16: Numerical experiment using physiological parameters: comparison of wall shear stresses for different Reynolds numbers, left: Re=114, right: Re=182, at two time instants $t = 0.36s$, $t = 0.96s$

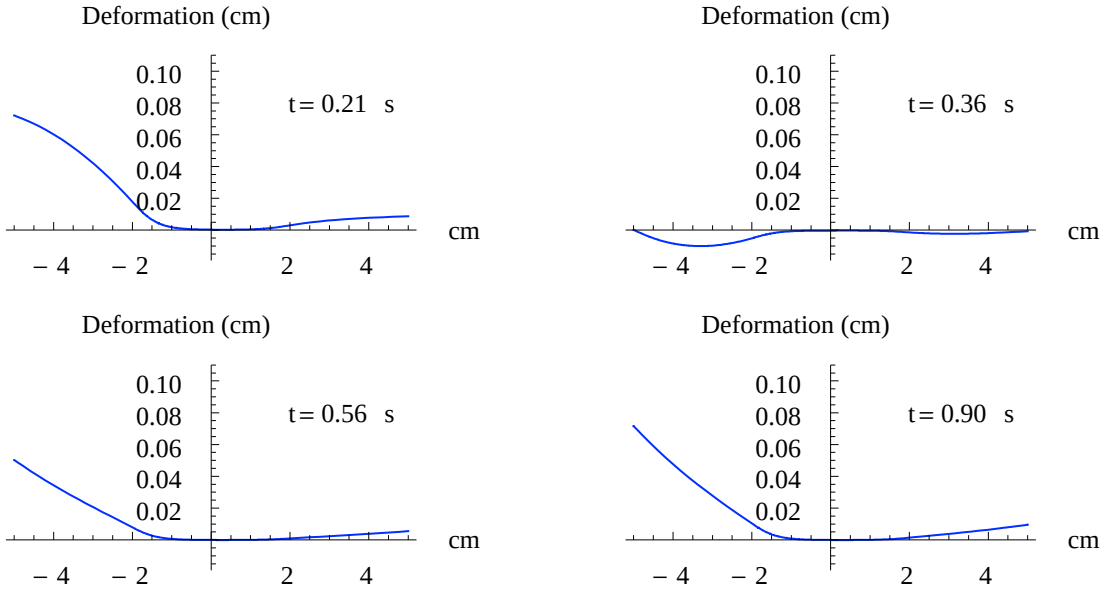

Figure 17: Numerical experiment with physiological parameters: wall deformation at four different time instants

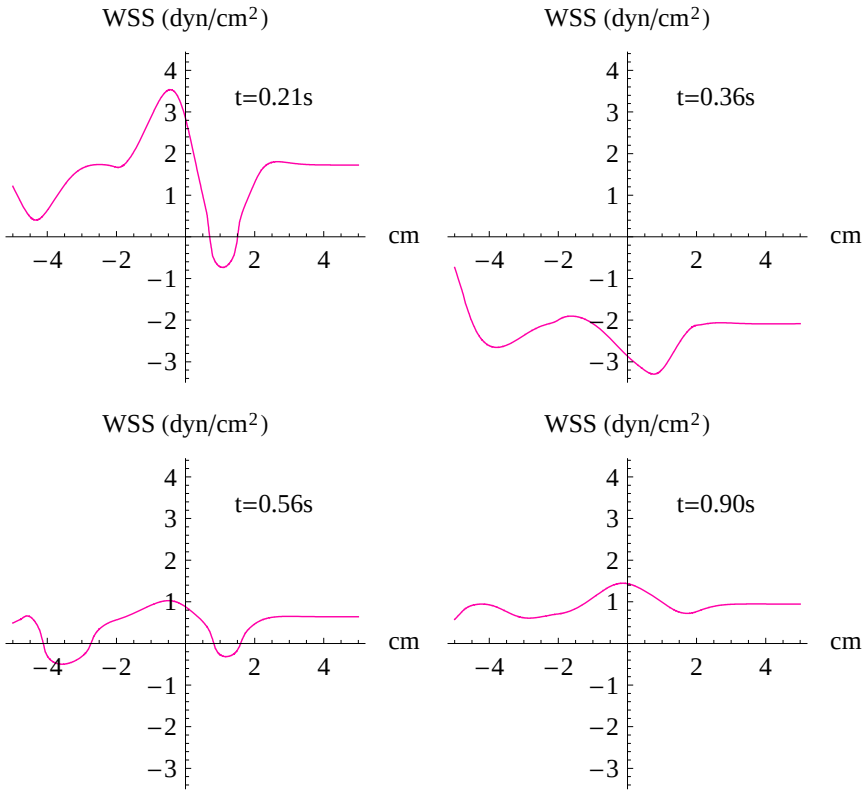

Figure 18: Wall shear stress at four different time instants

$t = 0.1s$

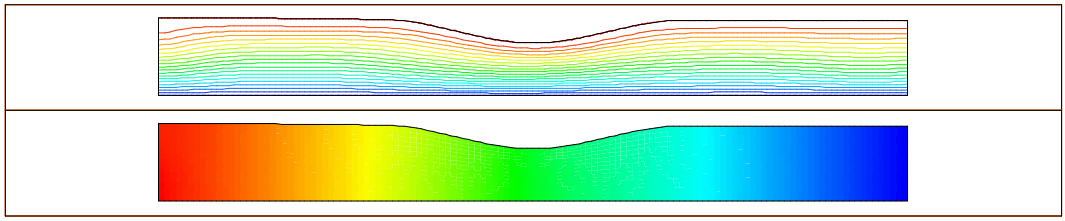

$t = 0.2s$

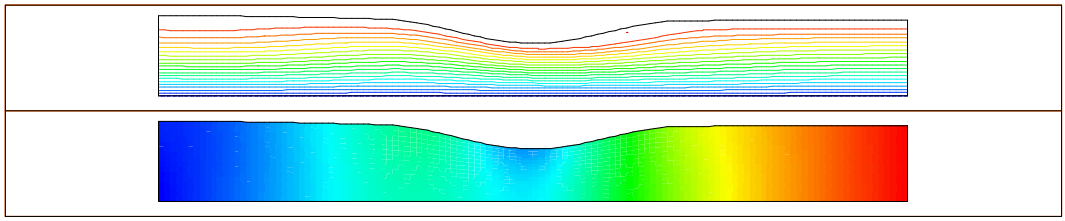

$t = 0.36s$

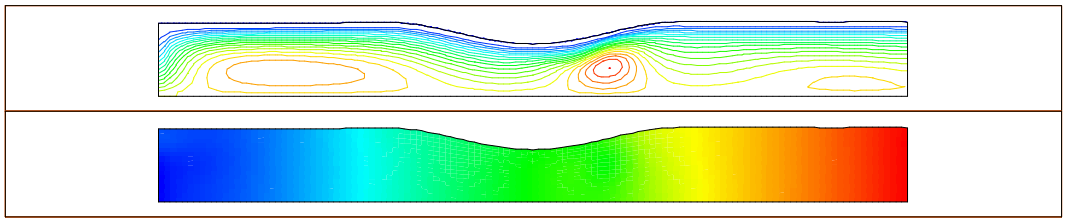

$t = 0.56s$

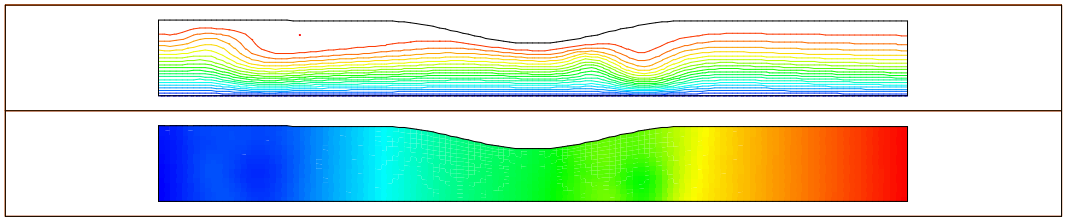

$t = 0.9s$

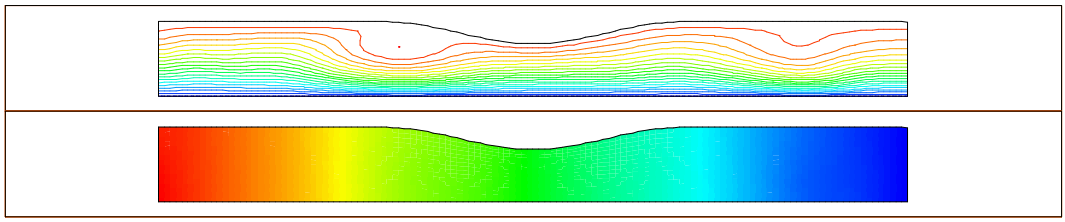

Figure 19: Streamlines and pressure at five different time steps $t = 0.1s$, $t = 0.2s$, $t = 0.36s$, $t = 0.56s$, $t = 9s$, Neumann boundary conditions at the end of vessels, damping in the stenotic region, iliac artery inflow

7 Convergence study

The aim of this chapter is to study the experimental order of convergence using the L^2 errors of solution at different meshes, cf. e.g. in [12]

$$EOC = log_2 \frac{\|\boldsymbol{u}_h - \boldsymbol{u}_{h/2}\|_{L^2}}{\|\boldsymbol{u}_{h/2} - \boldsymbol{u}_{h/4}\|_{L^2}},$$

where $\boldsymbol{u}_h$ is the solution on the mesh with mesh size h. We use also the notation

$$Err(\boldsymbol{u}_h) = \|\boldsymbol{u}_h - \boldsymbol{u}_{h/2}\|_{L^2}/|\Omega|, \quad Err(\eta_h) = \|\eta_h - \eta_{h/2}\|_{L^2}/2L,$$

analogously $Err(p_h)$ for pressure. The computational domain $\Omega(\eta)$ is consecutively divided into 16×2 elements (mesh 1.), 32×4 elements (mesh 2.), 64×8 elements (mesh 3.), 128×16 elements (mesh 4.), where the element size Δx and Δy is halved. We worked with piecewise linear approximation for fluid velocities and for pressure. For time discretization backward Euler method was used.

In Table 2 we present convergence order results for stationary flow in the rigid tube, see the Fig. 20 for the geometry and boundary conditions. In fact, the stationary flow has been simulated by time dependent equations that has been computed until the final time $T = 0.8s$. The non-Newtonian model (Carreau model, $\mu_\infty = 0.63,\ \mu_0 = 1.26,\ V_{inflow} = 38\,cm/s,\ q = -0.2$) has been compared to the Newtonian fluid ($\mu = 0.63,\ V_{inflow} = 38\,cm/s$). For velocity we have obtained the second order convergence in space for both the Newtonian as well as non-Newtonian flow. Let us note a reduced convergence rate for pressure in the non-Newtonian case that might be caused by the parabolic velocity profile in the Dirichlet boundary conditions. These are better suited for the Newtonian flow. In order to overcome this problem we have tested in what follows symmetry boundary conditions and Neumann outflow boundary conditions.

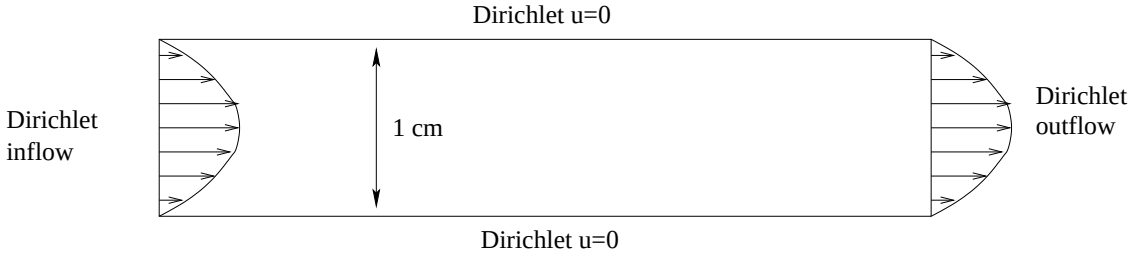

Figure 20: Boundary conditions in the 1. numerical experiment

Table 3 demonstrates convergence results on rigid halved domain with symmetry condition at the central line, see Fig. 21. We can notice slightly worse convergence rate in velocity for the Newtonian case. Moreover, in the non-Newtonian case the convergence in velocity is reduced to 1. This effect can be explained by the influence of symmetry boundary conditions coupled with the Neumann boundary conditions. On the other hand this boundary conditions improve convergence of pressure in the non-Newtonian case to

Table 2: Convergence order in rigid tube for Newtonian and non-Newtonian fluid

1. exp.	Newt. fluid $q = 0$				non-Newtonian fluid $q = -0.2$			
mesh	$Err(\boldsymbol{u}_h)$	EOC	$Err(p_h)$	EOC	$Err(\boldsymbol{u}_h)$	EOC	$Err(p_h)$	EOC
2/1	8.5771		22.881		9.3429		26.061	
3/2	1.4423	2.572	3.5120	2.704	1.5025	2.636	4.9486	2.397
4/3	0.2997	2.267	0.6934	2.341	0.2934	2.357	2.0053	1.303

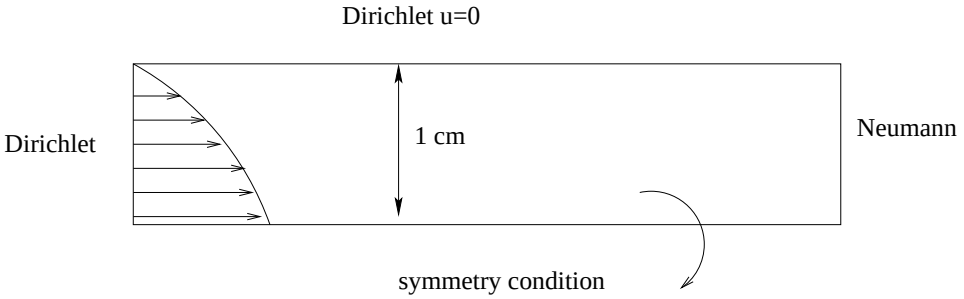

Figure 21: Boundary conditions in the 2. numerical experiment

the second order. Table 4 presents results for different exponent q, $q = -0.1$ and $q = -0.3$. Similarly, convergence order in velocity is reduced to 1.

Table 3: Convergence order in rigid tube

2. exp.	Newtonian fluid $q = 0$				non-Newt. fluid $q = -0.2$			
mesh	$Err(\boldsymbol{u}_h)$	EOC	$Err(p_h)$	EOC	$Err(\boldsymbol{u}_h)$	EOC	$Err(p_h)$	EOC
2/1	1.0783		3.5199		0.9859		3.7209	
3/2	0.2758	1.967	0.6870	2.357	0.2766	1.834	0.7073	2.395
4/3	0.0084	1.714	0.3204	1.101	0.1240	1.157	0.1577	2.165

In the following we will present numerical experiments for moving domain. We use halved domain with symmetry flow condition at the central line and the Neumann boundary condition at the outflow, see Fig. 21. Now, the flow is non-stationary and the final time was set to $T = 0.4s$. Eleven iterations of domain geometry has been performed in global framework (i.e. the values from previous domain iteration has been used in order to deform the domain in actual fluid-structure computation, as described in Section 5.1).

For Newtonian fluids, see Table 5 we observe almost second order convergence in velocity. Due to the reduced convergence rate in pressure we obtained also reduced convergence rate in the domain deformation η. The lower convergence rate for η as expected (we used Newmark scheme that has the second order accuracy) is thus caused by the worse con-

Table 4: Convergence order in rigid tube

2. exp.		non-Newt. fluid $q = -0.1$		non-Newt. fluid $q = -0.3$	
mesh	Δt	$Err(\boldsymbol{u}_h)$	EOC	$Err(\boldsymbol{u}_h)$	EOC
2/1	0.002	0.9307086		1.025074	
3/2	0.002	0.2627934	1.824	0.2806220	1.869
4/3	0.002	0.1207427	1.122	0.1131567	1.310

Table 5: Convergence order in deforming tube, $T = 0.4s$, $\mu = \mu_\infty = 0.63$

2. exp.	Newtonian fluid $q = 0$					
mesh	$Err(\boldsymbol{u}_h)$	EOC($\boldsymbol{u}_h$)	$Err(p_h)$	EOC(p_h)	$Err(\eta_h)$	EOC(η_h)
2/1	1.1078		3.3068		0.0065	
3/2	0.2831	1.968	0.6756	2.291	0.0021	1.6099
4/3	0.0862	1.714	0.3212	1.073	0.0009	1.2814

vergence of the pressure in the force term. Tables 6 and 7 present analogous numerical experiment for different exponents q, i.e. $q = -0.2$ and $q = -0.3$. Convergence rates in velocity and pressure are similar to those for non-Newtonian fluids in a rigid tube. As a consequence the second order convergence in pressure influences also the convergence of the domain deformation η, which is now of the second order as expected.

In conclusion in our future study we want to investigate the question of appropriate boundary condition more deeply. In particular, we want to derive boundary conditions suitable for both the Newtonian as well as non-Newtonian fluids, that will preserve the desired second order convergence in all components as well as in the domain deformation.

8 Conclusions

In this paper we have simulated blood flow in a part of elastic moving vessel and analyzed some hemodynamical control quantities. We have modeled blood as a shear-thinning non-Newtonian fluid and chosen two well-known models, the Carreau (or Carreau-Yasuda) model and the Yeleswarapu model. Comparisons with the Newtonian model are presented as well. We have investigated the wall deformation and the hemodynamical wall parameters, the wall shear stress WSS and the oscillatory shear index OSI for a straight and stenotic tube.

The fluid equations were approximated by the finite volume method with the pseudo-compressibility stabilization for spatial discretization. We have linearized the non-linear Cauchy stress tensor by fixed point iterations. For the deformation equation we used the Newmark finite difference scheme. The global iterations with respect to the domain

Table 6: Convergence order in deforming tube, $T = 0.4s$, $\mu_0 = 1.26$, $\mu_\infty = 0.63$

2. exp.	non-Newtonian fluid $q = -0.2$					
mesh	$Err(\boldsymbol{u}_h)$	EOC($\boldsymbol{u}_h$)	$Err(p_h)$	EOC(p_h)	$Err(\eta_h)$	EOC(η_h)
2/1	1.0194		3.4599		0.0074	
3/2	0.2825	1.851	0.6944	2.317	0.0023	1.696
4/3	0.1206	1.228	0.1556	2.158	0.0004	2.513

Table 7: Convergence order in deforming tube, $T = 0.4s$, $\mu_0 = 1.26$, $\mu_\infty = 0.63$

2. exp.	non-Newtonian fluid $q = -0.3$					
mesh	$Err(\boldsymbol{u}_h)$	EOC($\boldsymbol{u}_h$)	$Err(p_h)$	EOC(p_h)	$Err(\eta_h)$	EOC(η_h)
2/1	1.0558		3.3672		0.0068	
3/2	0.2850	1.889	0.5994	2.490	0.0019	1.840
4/3	0.1109	1.362	0.1522	1.977	0.0004	2.305

geometry are based on the ALE formulation for representation of the fluid-structure interaction. Numerical experiments indicate that the global iterative method is robust and relatively fast. The stability and accuracy of numerical method have been tested for several model parameters, including the physiological parameters for shear dependent viscosity and inflow rate.

The presented results demonstrate a significant influence of the non-Newtonian fluid model, especially for hemodynamical control quantities such as the WSS and OSI. Larger negative absolute values of WSS appears in the case of non-Newtonian fluids. According to some authors [16] this indicates the appearance of recirculation zones and reversal flows around stenosis, which seems to be better predicted by the non-Newtonian models. Further, the domain geometry has also a considerable influence on the wall deformation as well as on the WSS and OSI. Moreover the maximum values of OSI are larger for the non-Newtonian models in comparison to the Newtonian flow. Such high OSI values at the end of stenotic occlusion indicate a large oscillatory nature of the wall shear stress and could yield further to additional stenotic plug. Comparing the measurements of WSS and OSI for solid and compliant vessel we have obtained significantly higher oscillations of the wall shear stress for fixed solid vessels. This leads to the conclusion that the fluid-structure interaction aspect is important for hemodynamical modelling and should be involved in a reliable computational model.

Numerical experiments for viscosities with physiological parameters have been performed as well. We have shown that for higher Reynolds numbers the effects of non-Newtonian rheology are even more profound. All results confirm a significant influence of the fluid rheology and domain geometry on the wall deformation as well as on the hemodynamic wall parameters.

In future we want to extend the model and consider the generalized Oldroyd-B model that includes the viscoelastic properties of blood as well. Additionally, we want to consider different models for vessel walls, cf. [4] and more complex vessel geometries, e.g. bifurcations. Thus, we will not restrict ourselves only to the deformation in one direction but consider the domain deformation in both x_1 and x_2 direction, $\eta = (\eta_1, \eta_2)$. An important point of numerical simulation is a correct outflow boundary condition, reflecting the influence of the rest of the circulatory system. According to the [27] this can be realized by the so-called impedance condition arising from coupling the model with some less dimensional model (1D or 0D lumped model).

Theoretical analysis of similar problems for Newtonian fluids in a moving domain is presented e.g., in [28], [11], [5], [26], etc. Theoretical results of existence and uniqueness of the weak solution to our shear-dependent non-Newtonian fluid-structure problem have been presented in Section 4, see also [14]. However, we were able only to show existence and uniqueness of the solution for one global iteration. Our future goal is to show the convergence of global iterations that is indicated by our numerical experiments.

Acknowledgments: This research has been financed by the European Union's 6th Framework Programme Reference under the Contract no. DEASE: MEST-CT-2005-021122. The authors gratefully acknowledge this support.

References

[1] Bastian P, Johannsen K, Reichenberger V : *UG tutorial*, 2001

[2] Bodnár T., Sequeira A.: Numerical study of the significance of the non-Newtonian nature of blood in steady flow through a stenosed vessel. In R. Rannacher and Sequeira, A., editors, *Advances in Mathematical Fluid Mechanics* 83–104. Springer Verlag, 2010

[3] Broser PhJ : *Simulation von Strömungen in Blutgefässen*, Master's thesis, Ruprechts-Karl University, Heidelberg, 2001

[4] Čanić S, Tambača J, Guidoboni G, Mikelič A, Hartley CJ, Rosenstrauch D : Modelling viscoelastic behaviour of arterial walls and their intercation with pulsatile blood flow, *SIAM J. Appl. Math.* 67(1) (2006), 164–193.

[5] Chambolle A, Desjardin B, Esteban MJ, Grandmont C : Existence of weak solutions for unsteady fluid-plate interaction problem, *J. Math. Fluid Mech.* 7 (3) (2005), 368–404

[6] Černý J : *Numerical modelling of non-Newtonian flows with application in hemodynamics*, Report TU Hamburg-Harburg, 2004.

[7] Filo J, Zaušková A : 2D Navier-Stokes equations in a time dependent domain with Neumann type boundary conditions, *J. Math. Fluid Mech.* 10 (2008), 1–46

[8] Formaggia L, Gerbeau JF, Nobile F, Quarteroni A : On the coupling of 3D and 1D Navier-Stokes equations for flow problems in compliant vessels, *Computer Methods in Applied Mechanics and Engineering* 191 (6-7) (2001), 561–582

[9] Förster C, Scheven von M, Wall WA, Ramm E.: Coupling of incompressible flows and thin-walled structures In: *Coupled Problems 2007 International Conference on Computational Methods for Coupled Problems in Science and Engineering*, edited by Papadrakakis, M. and Onate, E. and Schrefler, B., Santori Island, Greece (2007) 541û544

[10] Gijsen FJH, van de Vosse FN, Janssen JD : Influence of the non-Newtonian properties of blood flow on the flow in large arteries: steady flow in a carotid bifurcation model, *J. Biomechanics* 32 (1999), 601–608

[11] Guidorzi M, Padula M, Plotnikov PI: Hopf solutions to a fluid-elastic interaction model, *Mathematical Models and Methods in Applied Sciences* 18 (2) (2008), 215–270

[12] Kröger T, Lukáčová-Medviďová M : An evolution Galerkin scheme for the shallow water magnetohydrodynamic equations in two space dimensions, *J. Computat. Phys.* 206 (2005), 122–149

[13] Lukáčová-Medviďová M, Černý J : Numerical modelling of non-Newtonian shear-thinning viscoelastic fluids with application in hemodynamics, *Proceedings of the Second International Symposium Modelling of Physiological Flows*, Portugal, (ed. Sequeira et al.), 2005

[14] Lukáčová-Medviďová M, Zaušková A : On the existence and uniqueness of non-Newtonian shear-dependent flow in compliant vessels, submitted to *SIAM J. Math. Anal* (2010), see also TUHH Preprints, https://www.mat.tu-harburg.de/ins/forschung/publikationen.php

[15] Lukáčová-Medviďová M, Zaušková A : Numerical modelling of shear-thinning non-Newtonian flows in compliant vessels, *Int. J. Numer. Meth. Fluids*, 56 (2008), 1409–1415

[16] Nadau L, Sequeira A : Numerical simulations of shear dependent viscoelastic flows with a combined finite element - finite volume method, *Computers and Mathematics with Applications* 53 (2007), 547–568

[17] Nägele S : *Mehrgitterverfahren für incompressiblen Navier-Stokes Gleichungen im laminaren und turbulenten Regime unter Berücksichtigung verschiedener Stabilisierungsmethoden*, PhD thesis, Ruprechts-Karl University, Heidelberg, 2003

[18] Málek J, Nečas J, Rokyta M, Ružička M : *Weak and Measure-Valued Solutions to Evolutionary PDEs*, Chapman and Hall, London, 1996

[19] Nobile F : *Fluid-structure interaction problems in hemodynamics*, Master's thesis, Technical University in Milan, 1998

[20] Quarteroni A : Fluid-structure interaction for blood flow problems, (*In Lecture notes on Simulation of Fluid and Structure Interaction*, AMS-AMIF Summer School, Prague), European Mathematical Society, 2001

[21] Perktold K, Rappitsch G : Mathematical modelling of local arterial flow and vessel mechanics, *Comput. Methods for Fluid-Structure Interaction* (1994), 230–245, Longman, Harlow

[22] Quarteroni A : Mathematical and numerical simulation of the cardiovascular system, *In Proceedings of the ICM*, 3 (2002), 839–850, Beijing

[23] Quarteroni A, Gianluigi R : Optimal control and shape optimization of aorto-coronaric bypass anastomoses, M^3 AS, *Mathematical Models and Methods in Applied Sciences* 23 (12) (2003), 1801–23

[24] Quarteroni A, Formaggia L : Mathematical modelling and numerical simulation of the cardiovascular system, *Handbook of Numerical Analysis* (P.G Ciarlet and J.L Lions Eds.), Elsevier, Amsterdam, 2002

[25] Rajagopal K, Lawson J : Regulation of hemostatic system function by biochemical and mechanical factors, Modeling of Biological Materials, Series: *Modeling and Simulation in Science, Engineering and Technology*, Birkhäuser, Boston (2007), 179–201

[26] Surulescu C : The instationary moion of a Navier-Stokes fluid through a vessel with an elastic cover, IWR Preprint, University of Heidelberg, 2005

[27] Taylor ChA, Vignon-Clementel IE, Figueroa CA, Jansenca, KE : Outflow boundary conditions for three-dimensional finite element modeling of blood flow and pressure in arteries, *Comput. Methods Appl. Mech. Engrg.* 195 (2006), 3776–3796

[28] Beirao da Veiga H : On the Existence of Strong Solution to a Coupled Fluid-Structure Evolution Problem, *J. Math. Fluid Mech.* 6 (1) (2001), 21–52

[29] Yeleswaapu KK : *Evaluation of continuum models for chatacterizing the constitutive behavior of blood* PhD thesis, University of Pittsburg, 1996

[30] Yeleswarapu KK, Kameneva MV, Rajagopal KR, Antaki JF : The flow of blood in tubes: theory and experiments, *Mech. Res. Comm.* 25 (3) (1998), 257–262

[31] Zaušková A : *2D Navier-Stokes equations in a time dependent domain.* PhD thesis, Comenius University, Bratislava, 2007